Article

Not peer-reviewed version

Mathematical Theory of Social Conformity II: Geometric Pinning, Curvature-Induced Quenching, and Curvature-Targeted Control in Anisotropic Logistic Diffusion

Dimitri Volchenkov *

Posted Date: 13 June 2025

doi: 10.20944/preprints202506.1136.v1

Keywords: anisotropic logistic diffusion; curvature-induced front quenching; targeted suppression control

 doi:10.20944/preprints202506.1136.v1

Article

Mathematical Theory of Social Conformity II: Geometric Pinning, Curvature-Induced Quenching, and Curvature-Targeted Control in Anisotropic Logistic Diffusion

Dimitri Volchenkov †

Department of Mathematics and Statistics, Texas Tech University, 1108 Memorial Circle, Lubbock, TX 79409, USA; dimitri.volchenkov@ttu.edu

† This paper is an extended version of our paper published in The 2025 International Conference on Nonlinear Science and Complexity hosted by the São Paulo State University & Federal University of São Paulo—UNIFESP on 4–8 August 2025, Rio Claro, Brazil.

Abstract: We advance a mathematical framework for collective conviction by deriving a continuum theory from the network-based model introduced in [1]. The resulting equation governs the evolution of belief through a degenerate anisotropic logistic–diffusion process, where diffusion slows as conviction saturates. In one spatial dimension, we prove global well-posedness, demonstrate spectral front pinning that arrests the spread of influence at finite depth, and construct explicit traveling-wave solutions. In two dimensions, we uncover a geometric mechanism of curvature-induced quenching, where belief propagation halts along regions of low effective mobility and curvature. Building on this insight, we formulate a variational principle for optimal control under resource constraints. The derived feedback law prescribes how to spatially allocate repression effort to maximize inhibition of front motion, concentrating resources along high-curvature, low-mobility arcs. Numerical simulations validate the theory, illustrating how localized suppression dramatically reduces transverse spread without affecting fast axes. These results bridge analytical modeling with societal phenomena such as protest diffusion, misinformation spread, and institutional resistance, offering a principled foundation for selective intervention policies in structured populations.

Keywords: anisotropic logistic diffusion; curvature-induced front quenching; targeted suppression control

PACS: 87.23.Ge, 82.40.Ck, 02.30.Yy

MSC: 35K57,35K65, 93C20

1. Introduction

Diffusive models of belief adoption, protest mobilization, and organizational change share a core intuition: *influence radiates outward through social ties but attenuates where saturation, resistance, or repression occur*. The present paper formalizes this intuition in a degenerate anisotropic logistic–diffusion framework (introduced by us in [1]) and analyses three geometric mechanisms: *one-dimensional pinning*, *two-dimensional curvature-induced quenching*, and *curvature-targeted control*. Before outlining the mathematical results, we motivate the study by surveying empirical domains in which these mechanisms manifest with striking regularity.

Protest diffusion and containment: Recent cross-national panel analyses covering more than thirty European states (2000–2015) reveal robust spatial contagion of protest: *unrest in one country raises both domestic and neighboring protest frequency in subsequent periods, producing travelling waves of contention*. Yet such waves rarely expand indefinitely. Data from the 2009–2010 Iranian Green Movement, the 2019

 doi:10.20944/preprints202506.1136.v1

Hong Kong demonstrations, and the 2020 Belarus protests show abrupt "arrests" of expansion after highly localised crack-downs, corridor blockades, or internet throttling, tactics that leave low-curvature arterial routes open but *pin* high-curvature flanks. The pattern echoes our one-dimensional analysis: *once a single depth layer of a protest hierarchy is saturated by repression, upward diffusion of mobilization stalls*.

Diffusion and suppression of misinformation: At the level of online discourse, large-scale Twitter studies demonstrate that false news diffuses more rapidly and broadly than factual information, often through a few high-degree hub accounts. Platform interventions increasingly adopt a geometry-aware approach, focusing resources on *hub* removal, flagging, or rate-limiting where the network curvature, informally, the concentration of potential diffusion paths, is highest. Experiments show that deleting or down-ranking a malicious post within thirty minutes can cut cumulative downstream engagement by over 90 %, whereas uniform throttling of all content achieves far less per unit effort. These findings parallel our two-dimensional quenching criterion: *targeting regions of maximal projected curvature offers disproportionate leverage*.

Organizational inertia and targeted dissent suppression: Inside bureaucratic hierarchies, information can likewise become "pinned". Morrison and Milliken's organizational-silence framework, replicated across corporate and governmental settings, shows that employees suppress negative feedback when punitive norms saturate a particular managerial layer, effectively halting upward flow of corrective signals. Recent fieldwork in United Nations peacekeeping departments reveals how "anticipatory obedience" concentrates along specific reporting corridors, quenching reform initiatives transversally while allowing day-to-day operations along the main vertical chain to proceed unchecked.

Historical precedents of strategic control: Eastern Germany's two-stage containment strategy (rapid arrest of focal organizers followed by selective media blackouts prior to construction of the Berlin Wall) illustrates curvature-targeted repression *avant la lettre*. Similarly, Soviet disaster archives on the Chernobyl accident document top-layer narrative pinning ("all systems normal") that froze internal dissent until the curvature of external scrutiny overwhelmed institutional inertia, precipitating a preference cascade.

These examples demonstrate that pinning, quenching, and curvature-sensitive control are not abstract artefacts but recurring features of social and political dynamics. Our goal is therefore twofold. First, we develop a minimal anisotropic logistic–diffusion model that captures the emergence and arrest of propagating fronts under nonlinear saturation and geometrically localized resistance. Second, we derive and analyze a variational principle for curvature–targeted control, identifying how limited repressive or corrective resources can be deployed to maximize suppression efficiency.

The subsequent sections are structured as follows: Sect. 2 introduces the probabilistic foundations of the underlying network–influence model; Sect. 3 derives its continuum limit and formulates the associated degenerate parabolic logistic equation; Sect. 4 establishes well-posedness and long-time behavior in the one-dimensional case; Sect. 5 investigates front selection and pinning phenomena; Sect. 6 extends the analysis to two dimensions, detailing curvature-induced quenching under anisotropic diffusion; Sect. 7 presents the optimal-control formalism and numerical illustrations; Sect. 8 interprets these mathematical results in light of empirical evidence from protest dynamics, organizational sociology, and digital media research; and Sect. 9 concludes with broader implications and directions for future work.

2. Probabilistic Foundations of the Network-Influence Model

Let a finite population of N agents be indexed by $i = 1, \dots, N$, each of whom is exposed to a particular informational proposition, social norm, innovation, or ideological stance, denoted collectively as a designated statement A. To formalize the adoption of A, we associate to each agent i a random variable $X_i \in \{0, 1\}$, where the event $X_i = 1$ signifies that agent i has accepted or internalized the statement. All probabilistic quantities introduced below are rigorously defined with respect to the canonical product probability space $(\Omega, \mathcal{F}, \mathbb{P})$ generated by the family $(X_1, \dots, X_N)$, where $\mathcal{F} = \sigma(X_1, \dots, X_N)$ is the minimal σ-algebra capturing joint distributions over all binary adoption states in the system.

 doi:10.20944/preprints202506.1136.v1

The prior probability that agent i independently adopts A prior to any social interaction or informational exchange is denoted $P_{0i} = \mathbb{P}\{X_i = 1 \mid \mathcal{F}_i^{\text{pri}}\}$, where $\mathcal{F}_i^{\text{pri}}$ is the agent-specific information field summarizing personal history, preferences, heuristics, and possibly exposure to external media or previous encounters.

To account for socially mediated influence, we introduce a row-stochastic matrix $\Lambda = (\lambda_{ji})$, where each entry $\lambda_{ji} \in [0,1]$ denotes the conditional probability that agent j takes agent i as an epistemic reference point when updating her belief. Structurally, Λ defines a weighted influence graph over the agent population, whereas probabilistically, it serves as a transition kernel for a Markov chain on the social network, reflecting the directional flow of informational trust. Each agent is further endowed with an individual-level parameter $\mu_j \in [0,1]$, representing *obstinacy*, i.e., the cognitive inertia or resistance to social influence. The posterior probability that agent j adopts A after a single equilibrium round of belief pooling is then given by the convex combination

$$P_j = \mu_j P_{0j} + (1 - \mu_j) \sum_{i=1}^{N} \lambda_{ji} P_{0i}, \tag{1}$$

which may be interpreted as the conditional probability $\mathbb{P}\{X_j = 1 \mid \mathcal{F}_j^{\text{post}}\}$ after integrating private priors with network-structured second-order beliefs, where $\mathcal{F}_j^{\text{post}}$ is the σ-algebra generated by agent j's direct observations of the prior beliefs held by her reference group as encoded in Λ. This expression extends classical DeGroot-type models [2] by allowing each agent to partially retain individual priors with strength μ_j, a feature empirically validated by studies in political psychology and communication science that associate increased obstinacy with ideological commitment, identity-protective cognition, and motivated reasoning [3,4].

In matrix notation, denoting by $P_0 \in \mathbb{R}^N$ the vector of prior adoption probabilities and by $M = \text{diag}(\mu_1, \ldots, \mu_N)$ the diagonal obstinacy matrix, we write the posterior update rule in fixed-point form as

$$P = MP_0 + (I - M)\Lambda P, \tag{2}$$

which resolves uniquely to the closed-form solution

$$P = SP_0, \quad \text{where} \quad S = [I - (I - M)\Lambda]^{-1} M. \tag{3}$$

The resolvent operator S encapsulates the cumulative outcome of all higher-order influence pathways over the social graph, incorporating iterated consensus-forming interactions under the constraint of individual obstinacy. Each entry S_{ij} may thus be interpreted as the marginal contribution of agent j's prior belief to agent i's stabilized posterior, and the operator S plays a central role in the subsequent dynamical model by fixing the weights of influence propagation in both discrete and continuous-time regimes.

Within the probabilistic framework described above, we distinguish two fundamentally different learning regimes based on the nature of exposure accumulation over time.

In the *fully correlated* (memory-preserving) regime, agents integrate all influence signals received from the onset of observation ($t = 0$) without any decay or reset, leading to temporally entangled adoption dynamics. Let $P_i(t) = \mathbb{P}\{X_i = 1 \text{ by time } t\}$ denote the cumulative probability of adoption for agent i after $t \in \mathbb{N}$ discrete rounds of exposure, each governed by the same influence operator S. Then the adoption probability satisfies the exact formula

$$P_i(t) = 1 - \int_{[0,1]^N} (1 - p_i)^t \left(\sum_{j=1}^{N} S_{ij} p_j \right) \prod_{j=1}^{N} dp_j, \tag{4}$$

as derived in [1], where the integral spans all possible configurations of prior belief probabilities $(p_1, \ldots, p_N) \in [0,1]^N$. This formulation captures the Bayesian updating of adoption likelihoods under perfect memory retention and statistical independence of priors across agents. The factor $(1 - p_i)^t$

 doi:10.20944/preprints202506.1136.v1

represents the cumulative probability that agent i has failed to adopt in t successive exposures, while the integrand weights this failure by the total social signal $\sum_j S_{ij} p_j$ received at each round. As $p_i \to 0$, the decay of $(1-p_i)^t$ becomes sub-exponential, resulting in heavy tails in the distribution of adoption times and the divergence of the expected learning time. Consequently, convergence in this regime is slow and strongly influenced by the global distribution of initial signals.

By contrast, the *memory-less* or Bernoulli–hazard regime assumes that each exposure event is statistically independent of prior ones, modeling probabilistic adoption as a continuous-time process governed by instantaneous hazard rates induced by socially aggregated influence. Letting $P_i(t) = \mathbb{P}\{X_i = 1 \text{ by time } t\}$ for $t \in \mathbb{R}_{\geq 0}$, we obtain the network-coupled nonlinear differential equation

$$\frac{dP_i}{dt} = (1 - P_i(t)) \sum_{j=1}^{N} S_{ij} P_j(t), \tag{5}$$

as derived in [1]. Here, $(1 - P_i(t))$ denotes the instantaneous probability that agent i remains unconverted at time t, while the aggregated influence $\sum_j S_{ij} P_j(t)$ represents the social pressure from already-adopting peers. The structure of the influence matrix S encodes both the topology and weighting of inter-agent effects.

Solutions $P_i(t)$ to equation (5) exhibit strictly monotonic and sigmoidal dynamics under general assumptions: namely, that S is nonnegative and irreducible and $P_i(0) \in (0, 1)$. Indeed, monotonicity follows since for all $t \geq 0$, both multiplicative factors on the right-hand side are positive, which implies that $P_i(t)$ is strictly increasing. The upper bound $P_i(t) < 1$ is maintained at finite time due to the vanishing of $(1 - P_i(t))$ as $P_i(t) \to 1$, and saturation occurs in the long-time limit: $\lim_{t\to\infty} P_i(t) = 1$. These properties confirm that $P_i(t) \in (0, 1)$ for all $t > 0$.

To rigorously establish the sigmoidal profile of the adoption trajectory $P_i(t)$, consider its second derivative:

$$\frac{d^2 P_i}{dt^2} = -\frac{dP_i}{dt} \sum_j S_{ij} P_j(t) + (1 - P_i(t)) \sum_j S_{ij} \frac{dP_j}{dt}. \tag{6}$$

Introducing the auxiliary quantities $A_i(t) = \sum_j S_{ij} P_j(t)$, and $B_i(t) = \sum_j S_{ij} \dot{P}_j$, we obtain the simplified form

$$\frac{d^2 P_i}{dt^2} = (1 - P_i(t)) \Big(B_i(t) - A_i(t)^2 \Big). \tag{7}$$

Since $P_j(t)$ is increasing and bounded, $B_i(t)$ initially grows faster than $A_i(t)^2$ but eventually lags behind as $P_j(t)$ flattens. Hence, there exists a critical time t^*, such that $\ddot{P}_i(t^*) = 0$, with $\ddot{P}_i > 0$ for $t < t^*$ and $\ddot{P}_i < 0$ for $t > t^*$. This confirms that $P_i(t)$ has a single inflection point and hence is sigmoidal. The logistic structure of (5), therefore, guarantees that all solution trajectories are smooth, strictly increasing, and exhibit a single peak in their growth rate. Consequently, the probabilistic interpretation of $P_i(t)$ as a cumulative hazard function remains valid, and the definition of the *mean learning time* (MLT) given by the first moment of the activation rate,

$$\bar{t}_i \equiv \int_0^\infty t \, \frac{dP_i(t)}{dt} \, dt, \tag{8}$$

is mathematically well-defined and directly applicable to the matrix-logistic dynamics. The quantity dP_i/dt in (5) thus serves as a valid probability density function on $\mathbb{R}_{\geq 0}$ for each agent's stochastic adoption time. The heterogeneous structure of S implies agent-dependent learning curves, which reflect both local influence topology and initial configuration.

The global behavior of belief propagation in the memory-less regime is ultimately governed by the spectral properties of the base conformity matrix Λ, which indirectly shapes the influence matrix S via (3). As a row-stochastic matrix, Λ admits a spectral decomposition $1 = \lambda_1 > |\lambda_2| \geq \cdots \geq |\lambda_N|$, where $\lambda_1 = 1$ corresponds to the trivial consensus eigenvalue, and the associated eigenvector is the invariant distribution π satisfying $\Lambda\pi = \pi$, $\sum_i \pi_i = 1$. The spectral gap $1 - |\lambda_2|$ controls the rate

 doi:10.20944/preprints202506.1136.v1

at which the discrete-time dynamics Λ^k converge to the rank-one projection $\mathbf{1}\pi^\top$. In the symmetric case (i.e., when Λ is reversible), this convergence is diffusive and uniform; in the asymmetric case, non-normality can lead to directional biases, transient amplification, or localization of influence. Obstinacy modulates this convergence by transforming the effective influence kernel to $(I - M)\Lambda$, scaling all nontrivial eigenvalues by factors bounded above by $1 - \mu_{\min}$. Consequently, obstinate agents resist rapid shifts in belief, leading to local smoothing but also global delays. This introduces a structural trade-off: while high obstinacy dampens local volatility and slows saturation, it can impede large-scale propagation, especially in sparse or weakly connected regions. This interplay between spectral structure, individual inertia, and global coordination speed will be quantitatively analyzed in subsequent sections, particularly through the lens of front velocity, saturation depth, and mean learning time.

3. Continuum Limit of the Matrix-Logistic Dynamics

We now derive the continuum limit of the matrix-logistic equation (5), which governs probabilistic adoption dynamics over a structured influence network. Consider a large-scale population embedded in a spatially regular lattice graph $G = (V, E)$, either one- or two-dimensional, with $N \gg 1$ nodes and uniform spacing $\delta x > 0$ such that $x_i = i\,\delta x$ defines the spatial position of node i. For a smooth adoption profile $u(x, t)$ interpolating the discrete probabilities $P_i(t)$, we assume that

$$P_i(t) \approx u(x_i, t), \tag{9}$$

in the limit $\delta x \to 0$. The influence matrix S is specified through the network structure and obstinacy parameters via Equation (3), and we assume that its entries correspond to a discrete diffusive kernel with locally varying coefficients, for instance,

$$S_{ij} \sim \frac{D(x_i)}{\delta x^2}\delta_{j=i\pm1}, \tag{10}$$

or more generally a smoothed convolution operator over local neighborhoods.

Under these assumptions, the aggregated influence term in (5) admits the diffusive approximation

$$\sum_{j=1}^{N} S_{ij}P_j(t) \approx D(x)\,\Delta u(x, t), \tag{11}$$

where $D(x)$ is a spatially dependent effective diffusion coefficient emerging from the composition of the local conformity weights Λ and obstinacy profile μ_i, and Δ is the Laplacian operator in the continuous spatial domain. Substituting into (5) and passing to the continuum limit yields the nonlinear degenerate diffusion equation

$$\partial_t u(x, t) = D(x)(1 - u(x, t))\,\Delta u(x, t). \tag{12}$$

This characterizes adoption under locally modulated persuasion and saturating nonlinearity. If the aggregated influence includes both diffusive dispersion and a mass amplification term, we assume

$$\sum_{j=1}^{N} S_{ij}P_j(t) = r(x)\,u(x, t) + D(x)\,\Delta u(x, t), \tag{13}$$

where $r(x)$ reflects autocatalytic amplification of beliefs in ideologically resonant regions. The resulting continuum model becomes a nonlinear logistic-diffusion PDE:

$$\partial_t u = D(x)(1 - u)\,\Delta u + r(x)\,u(1 - u). \tag{14}$$

 doi:10.20944/preprints202506.1136.v1

To interpret the coefficients $D(x)$ and $r(x)$, we expand the Neumann series for the influence matrix

$$S = M[I - (I - M)\Lambda]^{-1} \approx M\Big[I + (I - M)\Lambda + (I - M)^2\Lambda^2 + \dots\Big]. \tag{15}$$

In the regime of weak obstinacy $\mu_i \approx \mu \ll 1$, this yields $S \sim \mu\Lambda + \mu^2\Lambda^2 + \dots$, indicating a diffusive process governed by Λ. In the opposite limit $\mu_i \to 1$, we obtain $S \to I$, and the influence structure collapses to identity, halting propagation. Consequently, the coefficients are approximately

$$D(x) \sim \mu(x)\,\sigma^2(\Lambda), \qquad r(x) \sim \mu(x)\,\Lambda_{ii}, \tag{16}$$

where $\sigma^2(\Lambda)$ denotes a measure of the local spectral spread or diffusion strength encoded in Λ. To formalize this, let $\Lambda_{i\bullet}$ denote the i-th row of the conformity matrix, interpreted as a probability distribution over neighboring nodes. The local spectral spread at node i is then defined as the second spatial moment

$$\sigma^2(\Lambda)_i = \sum_{j=1}^{N} \lambda_{ij}(x_j - x_i)^2, \tag{17}$$

which quantifies the variance of the influence distribution around agent i. In regular lattices with uniform spacing δx, this yields $\sigma^2(\Lambda)_i \sim \delta x^2$, so the diffusion coefficient becomes $D(x_i) \sim \mu_i\,\delta x^2$, in agreement with classical finite-difference approximations of diffusive transport. For general graphs with spatial embeddings, $\sigma^2(\Lambda)_i$ characterizes the effective width of the influence kernel and reflects how broadly social influence disperses from each node.

In the continuum limit, belief dynamics synthesize two structurally distinct mechanisms: logistic self-reinforcement and saturation-limited diffusion. Both mechanisms admit closed-form traveling wave solutions, but only in the one-dimensional setting, where spatial ordering allows reduction to ordinary differential equations [5]. In higher-dimensional or networked domains, such explicit solutions generally fail, and front propagation becomes sensitive to geometry, anisotropy, and boundary effects. The analysis in [5] applies specifically to depth-ordered hierarchical structures, where a one-dimensional continuum approximation is valid.

The self-reinforcing component is governed by the classical Fisher–Kolmogorov–Petrovsky–Piskunov (FKPP) equation [6,7]:

$$\frac{\partial u}{\partial t} = D_f \frac{\partial^2 u}{\partial x^2} + ru(1 - u), \tag{18}$$

which supports traveling wave solutions $u(x,t) = U(x - v_F t)$ of sigmoidal form,

$$u(x,t) = \tfrac{1}{4}\Big[1 - \tanh\Big(x - v_F t + \tfrac{1}{v_F}\tanh^{-1}(-1 + 2\sqrt{u_0})\Big)\Big]^2, \tag{19}$$

with propagation speed

$$v_F = \tfrac{5\sqrt{6}}{6}\sqrt{D_f r}. \tag{20}$$

In contrast, the nonlinear diffusion mechanism is described by

$$\frac{\partial u}{\partial t} = D_f(1 - u)\frac{\partial^2 u}{\partial x^2}, \tag{21}$$

which degenerates as $u \to 1$, reflecting the inhibition of influence propagation in saturated regions. This equation admits an exact traveling wave solution [5] of the form $u(x,t) = 1 - f(\theta)$, where $\theta = \gamma x - \omega t + \theta_0$, given by $f(\theta) = -W\Big(-e^{-1-(\theta-\theta_*)}\Big)$, with $W(\cdot)$ denoting the principal branch of the Lambert function. Here, θ_0 represents a global phase shift determined by initial conditions, specifying the spatio-temporal location of the front, while θ_* denotes the internal coordinate at which the front reaches full saturation $f(\theta_*) = 1$. The difference $\theta_0 - \theta_*$ encodes the effective delay of front initiation

 doi:10.20944/preprints202506.1136.v1

and governs the onset position of activation in space-time. The normalization condition $\omega = D_f\gamma^2$ leads to the linear front velocity

$$v_{DD} = D_f\gamma, \tag{22}$$

in contrast to the square-root scaling of FKPP fronts (20). The resulting profile

$$u(x,t) = 1 + W\Big(-e^{-1-(\gamma x-\omega t+\theta_0-\theta_*)}\Big) \tag{23}$$

remains bounded in $[0,1]$ and rises monotonically for $\gamma x - \omega t + \theta_0 - \theta_* \geq 0$, describing a purely diffusive sigmoidal front with finite support and delayed activation.

4. One-Dimensional Degenerate Parabolic Logistic Models: Well-Posedness and Long-Time Behavior

In many applications of belief dynamics and saturation-limited propagation, particularly within hierarchical or tree-like network topologies, the underlying graph structure admits a natural depth stratification. Formally, if the interaction graph is a directed acyclic graph (DAG) $G = (V, E)$, a *layering* is a partition $V = \bigsqcup_{k=1}^{h} V_k$ such that every edge $(u, v) \in E$ respects the ordering $\mathrm{depth}(u) < \mathrm{depth}(v)$. This framework allows belief propagation models to be reformulated as effectively one-dimensional processes indexed by the discrete depth variable $k \in \mathbb{Z}_{\geq 1}$. Such a reduction is particularly well-suited to systems initiated by a fully convinced source agent, interpreted as a "teacher" node, anchored at the base level $k = 1$, with obstinacy $\mu_1 = 1$ and belief state fixed at $P_1(t) \equiv 1$ [5]. All downstream agents, positioned at greater depths $k \geq 2$, adopt uniform skeptical priors $P_k(0) = P_0 \ll 1$ and evolve under logistic belief dynamics governed by depth-dependent influences. In the continuum limit, this depth-indexed propagation reduces to a one-dimensional degenerate parabolic partial differential equation of logistic type, as analyzed in the present section.

4.1. Mathematical Formulation and Physical Interpretation

We investigate the nonlinear degenerate parabolic equation

$$\partial_t u = D(1-u)\,\partial_{xx}u + r\,u(1-u), \qquad u = u(x,t) \in [0,1], \tag{24}$$

posed on a bounded spatial domain $\Omega = (0, L) \subset \mathbb{R}$, equipped with homogeneous Neumann boundary conditions $\partial_x u|_{\partial\Omega} = 0$, ensuring conservation of total mass within the system. The parameters $D > 0$ and $r \geq 0$ denote the effective diffusivity and intrinsic reaction rate, respectively, and are treated as fixed throughout. The unknown scalar field $u(x,t)$ is normalized to lie within the physically admissible interval $[0,1]$, and is interpreted as a concentration variable subject to saturation constraints—for instance, encoding a belief level or occupancy probability, where $u = 0$ represents complete absence and $u = 1$ total saturation. The initial condition is assumed to satisfy $u_0 \in [0,1] \cap L^1(\Omega) \cap BV(\Omega)$, so that the initial profile is both integrable and of bounded variation, thereby admitting a well-defined weak formulation and ensuring compatibility with entropy methods. The principal structural feature of (24) is its degeneracy in the diffusive coefficient $a(u) \equiv D(1-u)$, which vanishes continuously as $u \to 1$. This degeneracy is multiplicative, in the sense of [8], as the diffusive flux takes the form $a(u)\,\partial_x u$, leading to a collapse of the ellipticity near saturation and rendering the classical De Giorgi–Nash–Moser theory [9–11] inapplicable cf. [8]. The effect is a spatially localized pinning of the diffusion process: regions where u approaches one become effectively frozen, halting the propagation of gradients and giving rise to finite-speed fronts and persistent saturated plateaux. This nonlinear interaction between reaction and degenerate diffusion constitutes the central mathematical challenge and physical richness of the model, which serves as a canonical paradigm for saturation-limited transport in heterogeneous media.

 doi:10.20944/preprints202506.1136.v1

4.2. Weak and Entropy Formulations for Degenerate Diffusion

To rigorously define the solution concept for (24), we first recast the equation in a conservative form by introducing the nonlinear flux and reaction terms

$$q(u) \equiv \int_0^u a(s)\,ds = D\Big(u - \tfrac{1}{2}u^2\Big), \qquad \mathfrak{f}(u) \equiv r\,u(1-u), \tag{25}$$

so that (24) becomes

$$\partial_t u + \partial_x(-a(u)\,\partial_x u) = \mathfrak{f}(u). \tag{26}$$

The degeneracy of the mobility $a(u) = D(1-u)$, which vanishes as $u \to 1$, precludes the direct use of standard elliptic regularity theory and necessitates a weak formulation in weighted Sobolev spaces. For a fixed function $u\colon \Omega \to [0,1]$, we define the weighted energy space

$$H^1_{a(u)}(\Omega) \equiv \left\{ v \in L^2(\Omega) \;\middle|\; \sqrt{a(u)}\,\partial_x v \in L^2(\Omega) \right\}, \tag{27}$$

equipped with the norm

$$\|v\|^2_{H^1_{a(u)}(\Omega)} \equiv \|v\|^2_{L^2(\Omega)} + \|\sqrt{a(u)}\,\partial_x v\|^2_{L^2(\Omega)}, \tag{28}$$

which captures the vanishing of diffusive transport in saturated zones. A function $u \in L^2_{\mathrm{loc}}([0,T); H^1_{a(u)}(\Omega)) \cap C([0,T); L^1(\Omega))$ is said to be a weak solution of (24) if it satisfies, for all test functions $\phi \in H^1(\Omega)$, the integral identity

$$\int_\Omega u(x,t)\,\phi(x)\,dx - \int_\Omega u_0(x)\,\phi(x)\,dx = \int_0^t \int_\Omega [a(u)\,\partial_x u\,\partial_x \phi + \mathfrak{f}(u)\,\phi]dx\,ds, \tag{29}$$

for almost every $t \in [0,T)$. While this definition is suitable for capturing energy dissipation and mass conservation, the presence of possible discontinuities in u, especially across sharp interfaces near saturation, motivates a more refined notion of solution that incorporates admissibility constraints via entropy inequalities.

Following the generalized entropy method pioneered by Kruzhkov [12] and subsequently extended to degenerate parabolic problems by Carrillo [13], and within nonlinear reaction–diffusion systems by Andreianov, Bendahmane, and Karlsen [14], we say that $u \in L^\infty([0,T); L^1(\Omega) \cap BV(\Omega))$ is an entropy solution of (24) if for every $k \in [0,1]$, the entropy pair

$$\eta(u) \equiv |u-k|, \qquad \eta'(u) \equiv \operatorname{sign}(u-k) \tag{30}$$

and the corresponding degenerate entropy flux

$$q_\eta(u) := \eta'(u)\,a(u)\,\partial_x u = \operatorname{sign}(u-k)\,D(1-u)\,\partial_x u \tag{31}$$

satisfy, in the sense of distributions on $\Omega_T := \Omega \times (0,T)$, the entropy inequality

$$\partial_t |u-k| + \partial_x q_\eta(u) \le \operatorname{sign}(u-k)\,\mathfrak{f}(u-k). \tag{32}$$

This inequality ensures that solutions are physically admissible and compatible with the irreversible character of the dynamics, particularly in the presence of shocks and saturation plateaux where classical derivatives may fail to exist. The entropy formulation implies L^1-contractivity of the solution semigroup, yields comparison principles under suitable initial data, and permits the derivation of uniqueness within the entropy class. Moreover, the entropy framework is robust under vanishing viscosity limits and aligns with numerical schemes designed to respect the structural degeneracy of

 doi:10.20944/preprints202506.1136.v1

the diffusion operator, thereby forming the cornerstone of the rigorous theory of nonlinear saturated transport models.

4.3. Friedrichs–Lax Regularisation and Approximate Solutions

In order to construct global-in-time solutions to the nonlinear degenerate parabolic Equation (24), we adopt a Friedrichs-Lax type regularisation scheme, which introduces a uniform ellipticity into the diffusive operator by perturbing the vanishing mobility near the saturated state. This procedure restores strict parabolicity and enables the derivation of energy estimates and compactness properties in a fully analytical setting [13,15,16]. For a fixed parameter $\varepsilon \in (0,1)$, we define a mollified mobility function that strictly bounds the diffusion coefficient away from zero:

$$a_\varepsilon(u) \equiv D[(1-u)+\varepsilon] = D(1-u+\varepsilon), \qquad \text{for } u \in [0,1], \tag{33}$$

which satisfies the uniform positivity condition $a_\varepsilon(u) \geq D\varepsilon > 0$ for all $u \in [0,1]$. The resulting regularized model reads

$$\partial_t u^\varepsilon + \partial_x(-a_\varepsilon(u^\varepsilon)\partial_x u^\varepsilon) = r\,u^\varepsilon(1-u^\varepsilon), \qquad u^\varepsilon(x,0) = u_0(x), \quad \partial_x u^\varepsilon|_{\partial\Omega} = 0, \tag{34}$$

posed on a bounded spatial domain $\Omega \subset \mathbb{R}$ under homogeneous Neumann boundary conditions. These guarantee the conservation of total mass and prevent flux across the boundaries. The essential idea is that while the original degeneracy $a(u) = D(1-u) \to 0$ as $u \to 1$ introduces analytic difficulties associated with loss of regularity and compactness, the approximation $a_\varepsilon(u)$ retains the qualitative features of the degeneracy while avoiding pathological vanishing. This structure allows for multiple numerical and analytical approximations. In particular, equation (34) may be discretized using a monotone Lax–Friedrichs finite-difference scheme [15,16], wherein the artificial viscosity arising from numerical fluxes regularizes potential shock formation and ensures stability in the sense of bounded total variation [17]. Alternatively, the same equation can be approximated using a semi-discrete Galerkin method, in which the diffusive term is augmented by an explicit artificial viscosity $\delta\partial_{xx}u^\varepsilon$, where the vanishing parameter $\delta = \delta(h) \to 0$ depends on the spatial mesh size $h \to 0$ [13,18]. Both approaches yield global-in-time, smooth classical solutions $u^\varepsilon \in C^\infty(\overline{\Omega_T})$, which are uniformly bounded and lie in the physical interval $[0,1]$ under appropriate Stampacchia-type truncation arguments. These regularized solutions serve as the analytic backbone for deriving uniform a priori estimates, entropy inequalities, and compactness results required for the passage to the singular limit $\varepsilon \to 0$, wherein weak or entropy solutions to the original degenerate problem are recovered. This framework, rooted in classical treatments of degenerate parabolicity, provides a robust methodological bridge between strictly parabolic approximation schemes and the multiplicatively degenerate limiting equation, and forms a key analytic step in the proof of well-posedness for nonlinear belief propagation models under saturation constraints.

4.4. Entropy Dissipation and A Priori Estimates

Uniform a-priori estimates for the approximate solutions $u^\varepsilon \in C^\infty(\overline{\Omega_T})$ of the regularised equation (34) are obtained via the entropy method of Bénilan–Crandall [19], based on a strictly convex Lyapunov functional adapted to the degeneracy structure. For each $\varepsilon > 0$, define the regularised mobility $a_\varepsilon(u) := D(1-u+\varepsilon)$, and introduce the convex entropy potential

$$\Phi_\varepsilon(u) := \int_0^u \int_0^s \frac{1}{a_\varepsilon(\sigma)}\, d\sigma\, ds, \tag{35}$$

so that $\Phi_\varepsilon''(u) = a_\varepsilon(u)^{-1} > 0$, uniformly on $[0,1]$. Multiplying (34) by $\Phi_\varepsilon'(u^\varepsilon) \in C^1([0,1])$ and integrating by parts over Ω yields the entropy dissipation identity:

$$\frac{d}{dt}\int_\Omega \Phi_\varepsilon(u^\varepsilon)\,dx + \int_\Omega a_\varepsilon(u^\varepsilon)\,|\partial_x u^\varepsilon|^2\,dx = r\int_\Omega u^\varepsilon(1-u^\varepsilon)\,\Phi_\varepsilon'(u^\varepsilon)\,dx. \tag{36}$$

 doi:10.20944/preprints202506.1136.v1

The right-hand side of (36) is nonpositive due to the sign structure of the product $u^\varepsilon(1-u^\varepsilon)\Phi_\varepsilon'(u^\varepsilon)$: for $u \in [0,1]$, the reaction term $f(u) = ru(1-u)$ is nonnegative for $u \in [0, \frac{1}{2}]$, nonpositive for $u \in [\frac{1}{2}, 1]$, and Φ_ε' is strictly increasing, so that the product is everywhere bounded above by zero. Hence, for all $t \in [0,T]$, the entropy is non-increasing:

$$\sup_{t\in[0,T]} \int_\Omega \Phi_\varepsilon(u^\varepsilon(x,t))\,dx \le \int_\Omega \Phi_\varepsilon(u_0(x))\,dx. \tag{37}$$

Moreover, the second term in (36) yields coercive control of the weighted gradient,

$$\int_0^T \int_\Omega a_\varepsilon(u^\varepsilon)\,|\partial_x u^\varepsilon|^2\,dx\,dt < \infty, \tag{38}$$

which implies $\sqrt{a_\varepsilon(u^\varepsilon)}\,\partial_x u^\varepsilon \in L^2(\Omega_T)$. Consequently, the approximate solutions u^ε are uniformly bounded in the reflexive space

$$L^2(0,T;H^1_{a_\varepsilon}(\Omega)) := \left\{ v \in L^2(0,T;L^2(\Omega)) \;\middle|\; \sqrt{a_\varepsilon(u^\varepsilon)}\,\partial_x v \in L^2(\Omega_T) \right\}, \tag{39}$$

and the time derivatives $\partial_t u^\varepsilon$ are controlled in $L^2(0,T;H^{-1}(\Omega))$ via testing the weak form of (34) against functions in $H^1(\Omega)$. By the Aubin–Lions lemma [20,21], applied in the compact embedding

$$H^1_{a_\varepsilon}(\Omega) \hookrightarrow\hookrightarrow L^1(\Omega) \hookrightarrow H^{-1}(\Omega), \tag{40}$$

this yields strong precompactness of $\{u^\varepsilon\}_{\varepsilon>0}$ in $L^1(\Omega_T)$. The dissipation identity (36) thus plays a central role in controlling the nonlinear fluxes and establishing convergence of the regularised sequence to an entropy solution of the original degenerate problem (24).

4.5. Compactness and Limit Passage to Entropy Solutions

Uniform a priori bounds derived from the entropy dissipation identity (36) and Stampacchia truncation [22,23] imply compactness of the regularised sequence $\{u^\varepsilon\}_{\varepsilon>0} \subset C^\infty(\overline{\Omega_T})$ in $L^1(\Omega_T)$. The pointwise maximum principle yields

$$0 \le u^\varepsilon(x,t) \le 1 \quad \text{for a.e. } (x,t) \in \Omega_T, \tag{41}$$

ensuring confinement to the admissible interval. Integration of the regularised equation (34) under homogeneous Neumann boundary conditions provides the mass decay estimate

$$\frac{d}{dt}\int_\Omega u^\varepsilon(x,t)\,dx = r\int_\Omega u^\varepsilon(1-u^\varepsilon)\,dx \le 0, \tag{42}$$

yielding uniform boundedness in $L^\infty(0,T;L^1(\Omega))$. A weighted Poincaré inequality [24], applied to the dissipation structure, implies bounded variation:

$$\int_\Omega |\partial_x u^\varepsilon(x,t)|\,dx \le C\left(\int_\Omega a_\varepsilon(u^\varepsilon)|\partial_x u^\varepsilon|^2 dx\right)^{1/2}, \tag{43}$$

with the right-hand side uniformly bounded in $L^2(0,T)$ due to the entropy decay (36) [19]. Temporal regularity follows from the differential Bénilan–Crandall inequality:

$$\iint_{\Omega_T} |u^\varepsilon - k|\,\partial_t\psi\,dx\,dt + \iint_{\Omega_T} \operatorname{sgn}(u^\varepsilon - k)\,a_\varepsilon(u^\varepsilon)\,\partial_x u^\varepsilon\,\partial_x\psi\,dx\,dt \ge 0, \tag{44}$$

 doi:10.20944/preprints202506.1136.v1

valid for all $k \in (0,1)$, $\psi \in C_c^\infty(\Omega_T)$, $\psi \geq 0$, which guarantees equi-continuity in time in the negative Sobolev space $H^{-1}(\Omega)$. Applying the Aubin–Lions–Simon lemma [20,21] in the compact embedding scale $H^1_{a(u)}(\Omega) \hookrightarrow L^1(\Omega) \hookrightarrow H^{-1}(\Omega)$, one obtains

$$u^\varepsilon \to u \quad \text{strongly in } L^1(\Omega_T), \quad \text{up to a subsequence}, \tag{45}$$

and almost everywhere convergence. To justify the limit passage in the nonlinear diffusion term, one invokes the Minty–Browder monotonicity trick [25,26], yielding

$$a_\varepsilon(u^\varepsilon)\,\partial_x u^\varepsilon \rightharpoonup a(u)\,\partial_x u \quad \text{weakly in } L^1(\Omega_T), \tag{46}$$

with $a(u) = D(1-u)$, while lower semicontinuity ensures that the limit function u inherits the bounds (41)–(43). Uniqueness follows by Kruzhkov's doubling-of-variables method [12], adapted to the degenerate flux $q(u) = D(u - \frac{1}{2}u^2)$. Testing with mollified indicators $\varphi_\delta(x-y)\eta_\delta(t-s)$, one obtains the L^1-contraction estimate

$$\|u(t) - v(t)\|_{L^1(\Omega)} \leq \|u_0 - v_0\|_{L^1(\Omega)} \quad \forall t \in [0,T], \tag{47}$$

which ensures that the limit $u \in L^\infty([0,T]; L^1(\Omega)) \cap BV(\Omega_T)$ is the unique entropy solution of the original degenerate initial-boundary value problem (24). This compactness and convergence analysis, together with the a priori entropy bounds and structural dissipation, provides a rigorous well-posedness framework for the multiplicatively degenerate logistic–diffusion system, as developed in [13,14,19].

4.6. Stability and Saturation Fronts in Entropy Dynamics

Central to the well-posedness of the degenerate logistic–diffusion equation is an L^1-contraction principle extending Kruzhkov's theory [12] to nonlinear fluxes with degenerating mobility $a(u) = D(1-u)$, which vanishes at $u = 1$. Let u, v be entropy solutions with initial data $u_0, v_0 \in [0,1] \cap L^1 \cap BV$. Testing the entropy inequalities with the Kruzhkov pair $\eta(u,k) = |u-k|$, $\eta'(u) = \operatorname{sgn}(u-k)$, and its counterpart for v, summing the resulting relations, and exploiting the concavity of the primitive flux $q(u) = D(u - \frac{1}{2}u^2)$, together with the Lipschitz monotonicity of the reaction $f(u) = ru(1-u)$, yields the differential estimate

$$\frac{d}{dt}\,\|u(\cdot,t) - v(\cdot,t)\|_{L^1(\Omega)} + \int_\Omega \big[a(u) + a(v) - 2a(\widehat{u,v})\big]\,\big|\partial_x(u-v)\big|\,dx \;\leq\; 0, \tag{48}$$

where $\widehat{u,v} = \max\{u,v\}$. Since the bracketed term satisfies $a(u) + a(v) \geq 2a(\widehat{u,v})$ by subadditivity of $a = q'$, the second integral is non-negative and may be discarded, yielding the strict contraction estimate $\|u(\cdot,t) - v(\cdot,t)\|_{L^1} \leq \|u_0 - v_0\|_{L^1}$ for all $t > 0$; cf. [12,13]. Choosing v as a supersolution with $v_0 \geq u_0$ furnishes the comparison principle $u(x,t) \leq v(x,t)$, while the degeneracy of $a(u)$ precludes interior attainment of the saturated state $u = 1$. Indeed, if $u(x_0,t_0) = 1$ at an interior point, then the flux $-a(u)\,\partial_x u$ vanishes identically in a neighbourhood, and the saturated plateau propagates with finite speed governed by the travelling-wave reduction

$$-c\,U'(\xi) = a(U(\xi))\,U''(\xi) + r\,U(\xi)(1 - U(\xi)), \qquad \xi = x - ct, \tag{49}$$

whose phase-plane analysis reveals a critical half-width beyond which no monotone front connects $u = 1$ to lower values, implying front pinning [5]. The contraction estimate (48), combined with the positivity of the approximate solutions from the regularised scheme, guarantees uniqueness of entropy solutions in the class $L^\infty(0,T; BV(\Omega)) \cap C([0,T]; L^1(\Omega))$, and continuous dependence on the data (u_0, D, r) in the L^1-metric, thereby completing the stability theory for the degenerate parabolic model (24).

Although the degenerating coefficient $a(u) = D(1-u)$ annihilates the classical Krylov–Safonov machinery [27] at saturation, the combination of BV-compactness and weighted elliptic regularity [8]

 doi:10.20944/preprints202506.1136.v1

ensures instantaneous spatial smoothing away from the plateau set $\{u = 1\}$. For every $t_0 > 0$, the distributional gradient satisfies $\partial_x u(\cdot, t) \in L^1(\Omega)$ for all $t \geq t_0$, implying $u(\cdot, t) \in BV(\Omega)$ and, via the Morrey embedding [28], interior Hölder continuity with exponent and constant deteriorating algebraically near $\{u = 1\}$ [8]. The argument refines the weighted Caccioppoli inequality of Bénilan–Crandall [19] by incorporating the Lyapunov weight $(1-u)^{-\beta}$, followed by Alikakos iteration [29] in the spirit of DiBenedetto–Friedman [30], though without invoking the De Giorgi–Nash theorem [9,10], which fails under multiplicative degeneracy [8]. It follows that for every compact $K \Subset \{x \in \Omega : \sup_{s \geq t_0} u(x,s) < 1\}$, there exists $\alpha \in (0,1)$ such that $u \in C^{1+\alpha}(K \times [t_0, \infty))$, whereas no Hölder gain is possible where u reaches unity, a rigidity underpinning the pinning effect.

Long-time dynamics are governed by the entropy functional

$$E[u(t)] = \int_\Omega Q\big(u(x,t)\big)\, dx, \qquad Q'(s) = -\log(1-s), \tag{50}$$

whose evolution along entropy solutions satisfies the dissipation identity

$$\frac{d}{dt} E[u(t)] + \int_\Omega \frac{D(1-u)}{1-u} \, |\partial_x u|^2 \, dx + r \int_\Omega u(1-u)\, \log(1-u)\, dx = 0, \tag{51}$$

so that $E[u(t)]$ is non-increasing and coercive in L^1. If the initial mass of the unsaturated region, $\int_\Omega (1-u_0)\, dx$, is strictly positive but sufficiently small, the reaction term dominates and the solution converges exponentially to the homogeneous state $u \equiv 1$. Conversely, if the saturated support $\{x : u_0(x) = 1\}$ contains an interval longer than the critical diffusion length $L_c \simeq \sqrt{D/r}$, the entropy identity (51) admits steady minimisers with pinned plateaus, and the solution converges algebraically to such heterogeneous equilibria, the decay rate determined by the spectral gap of the linearised arrest operator. These decay estimates reinforce the earlier uniqueness result and clarify the dynamical dichotomy between full consensus and finite-speed stagnation.

Extending this analysis to higher spatial dimensions, anisotropic diffusivity tensors $D_{ij}(x)$, or additional advective drifts $b(x)\partial_x u$ presents significant challenges: the loss of one-dimensional order invalidates Kruzhkov's flux-pair construction, the weighted BV-framework becomes vectorial, and accurate numerics must resolve evolving pinning interfaces governed by a free-boundary problem coupled to the degenerate parabolic core. These are topics to be addressed in future work.

The analytical framework developed above rigorously establishes the well-posedness, regularity, and long-time behavior of entropy solutions to the degenerate parabolic logistic equation (24). The interplay between structural degeneracy, entropy dissipation, and finite-speed propagation leads to a rich phenomenology of pinning and stagnation that departs fundamentally from classical diffusion-reaction models. The convergence theory, built on compactness and monotonicity tools, not only affirms existence and uniqueness in low regularity classes but also sets the stage for further investigations into multidimensional degeneracies, anisotropic fluxes, and free-boundary evolutions associated with saturated fronts.

5. Pinning and Front Selection in One Dimension

In this section, we develop a rigorous theory of front propagation in the one-dimensional degenerate logistic–diffusion model (24), focusing on two dynamically distinct mechanisms: (i) the emergence and spatial localization of pinned plateaus near saturation; and (ii) the nonlinear selection of front velocity via matched asymptotics between the weak-signal and degenerate regions. The mobility coefficient $D(1-u)$ vanishes near saturation and encodes the mechanism of spontaneous arrest. As shown below, any saturated point $u(x_0, t_0) = 1$ initiates a region of finite-speed propagation governed by the travelling-wave reduction (49), whose phase-plane structure reveals a critical half-width below which no admissible front can connect the saturated and unsaturated states [5].

 doi:10.20944/preprints202506.1136.v1

We define a *pinned plateau* as a nontrivial interval on which the solution remains saturated irreversibly. More precisely, for some $t_0 > 0$ and interval $(x_-, x_+) \subset \mathbb{R}$,

$$u(x, t_0) = 1 \text{ for } x \in (x_-, x_+) \quad \Longrightarrow \quad u(x, t) \equiv 1 \text{ for } t \geq t_0,\ x \in (x_-, x_+), \tag{52}$$

since the flux $-D(1-u)\,\partial_x u$ vanishes identically at saturation [19]. In the sociophysical interpretation of (24), this corresponds to a *frozen-conviction zone*: a saturated agent cluster becomes dynamically inert, and external influence cannot penetrate it. The domain splits into an active sector $u < 1$, where diffusion operates, and a pinned core whose survival depends on initial overshoot and the ratio D/r.

A refined maximum principle explains the irreversibility of such plateaux. Let u be a bounded weak solution, and suppose $u(x_0, t_0) = 1$ is achieved in the interior. The degeneracy annihilates diffusion, and evaluating the PDE yields

$$0 \leq \partial_t u(x_0, t_0) = D(1-u)\,\partial_{xx} u + r\,u(1-u) = 0, \tag{53}$$

so that all inequalities are saturated. The strong maximum principle [8,19] then forces $u \equiv 1$ in a neighborhood, and unique continuation implies persistence. A sharp threshold follows from matched asymptotics: equating the exponential tail $U(\xi) \sim e^{-\gamma\xi}$, where $\gamma^2 = r/D$, to the interior curvature scale yields the minimal half-width

$$L_c \simeq \sqrt{\frac{D}{r}}, \tag{54}$$

so that initial plateaus of width less than $2L_c$ vanish, while wider ones persist.

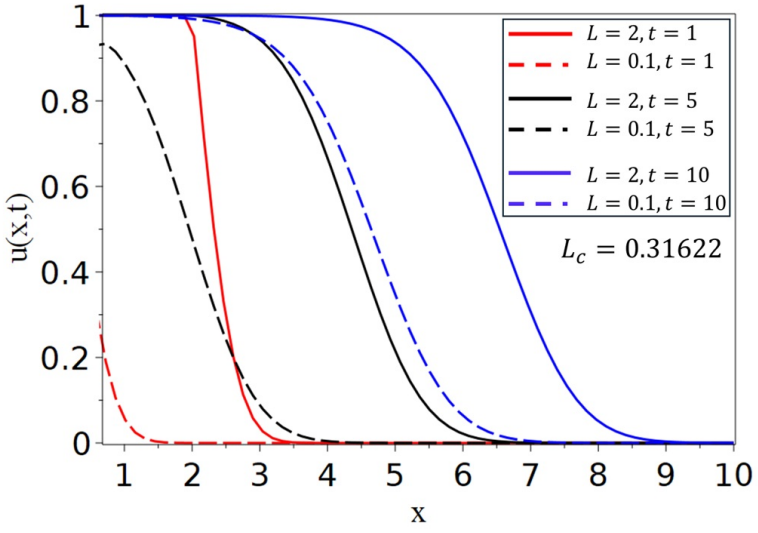

Figure 1. Time evolution of $u(x,t)$ with initial condition $u_0(x) = \mathbf{1}_{[0,L]}(x)$ for $L = 2 > L_c \approx 0.316$ (solid) and $L = 0.1 < L_c$ (dashed). Supercritical plateaux propagate; subcritical ones decay.

Further insight comes from the phase portrait of the travelling-wave system. Setting $V = U'$, equation (49) becomes

$$U' = V, \quad V' = -\frac{c + r(1-U)}{D(1-U)}\,V, \tag{55}$$

with degenerate saddle at $(U, V) = (1, 0)$. Linearization reveals one zero and one diverging eigenvalue, placing the origin on a non-hyperbolic center manifold. Centre-manifold theory [31] shows that orbits launched at $U = 1$ remain pinned, while those with $U < 1$ escape immediately. The entire segment $\{U = 1, V = 0\}$ is invariant, structurally enforcing pinning.

Numerical integration confirms this: given a saturated initial patch, the edge recedes at finite velocity $c_{\text{pin}}(D, r)$, and the interior remains flat. Rescaling $\xi \mapsto \xi/\sqrt{Dt}$ collapses interface profiles to

 doi:10.20944/preprints202506.1136.v1

a similarity shape, consistent with the law $x_{\text{edge}}(t) \sim x_0 \pm 2\sqrt{Dt}$. Motion halts precisely when the profile shrinks to size $2L_c$, after which the segment remains permanently pinned.

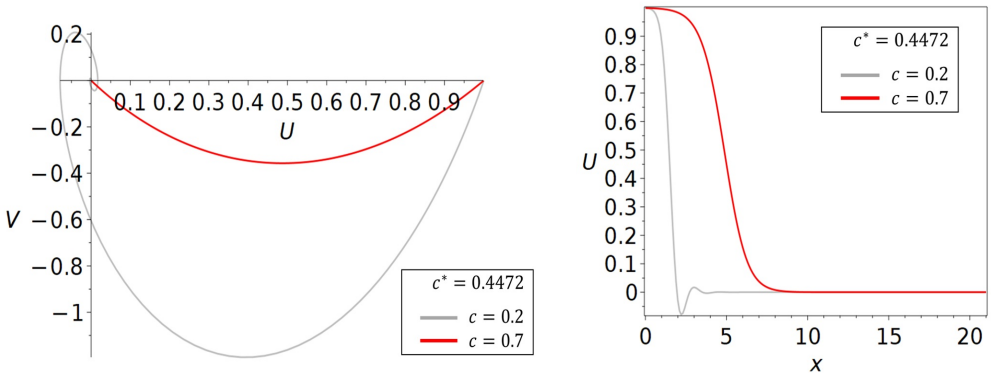

Figure 2. (a) Phase-plane trajectories for $c = 0.2 < c^* \approx 0.447$ (grey, unstable) and $c = 0.7 > c^*$ (red, admissible). **(b)** Corresponding profiles $U(x)$. Subcritical waves violate monotonicity and positivity; supercritical ones yield valid fronts.

Finally, we examine front selection numerically. The critical velocity $c^* = 2\sqrt{Dr}$ arises from linearization at the leading edge and marks the pulled/pushed transition. Subcritical waves violate monotonicity and decay conditions, while supercritical ones connect $U = 1$ to $U = 0$ smoothly. Figure 2 confirms this dichotomy. Thus, despite the absence of spectral bifurcations, the system exhibits sharp thresholds: L_c for plateau survival, and c^* for admissible propagation.

This completes the analytic picture: pinned regions emerge and persist due to degeneracy, propagation occurs when saturation is sufficient, and coherent fronts exist only when their speed exceeds the linear threshold. No instability or bifurcation was observed; hence, the degenerate logistic–diffusion model in one dimension admits only robust, threshold-governed dynamical regimes.

6. Two–Dimensional Geometry, Anisotropy and Curvature–Induced Quenching in Degenerate Parabolic Logistic Models

We now turn to the analysis of degenerate logistic belief propagation in spatial domains of dimension $d = 2$, focusing on geometric and tensorial extensions of the one-dimensional dynamics studied previously. In higher dimensions, the propagation of conviction fronts becomes sensitive not only to the degeneracy structure $D(x, y)(1 - u)$, which encodes saturation-induced diffusion arrest, but also to anisotropy arising from the directional asymmetries of the influence network.

The motivating discrete structure is depicted in Figure 3, and consists of a two-dimensional directed grid of agents arranged on a square lattice augmented by diagonal links, forming a full 8-neighbor Moore-type connectivity pattern. Each node $i \in V$ influences its immediate neighbors in the horizontal, vertical, and diagonal directions, with direction-dependent conformity weights as indicated. The central node at spatial index $(0, 0)$, marked in red, acts as a fully convinced teacher: its belief state is fixed at unity and its obstinacy coefficient normalized as $\mu_{(0,0)} = 1$. All other agents share homogeneous low obstinacy $\mu \ll 1$, and evolve under the matrix logistic dynamics. This configuration defines a canonical anisotropic two-dimensional influence network whose macroscopic limit inherits both degeneracy and directional asymmetry.

We define the influence matrix S via the posterior amplification structure (3), with homogeneous obstinacy $\mu \ll 1$ for all $(m, n) \neq (0, 0)$, and full Moore-type neighborhood weighted by direction-dependent conformity coefficients. For each node $i = (m, n)$, the matrix element $S_{i,j}$ is nonzero only if $j \in \mathcal{N}_{m,n}$, where $\mathcal{N}_{m,n}$ denotes the ordered list of horizontal, vertical, and diagonal predecessors of i,

 doi:10.20944/preprints202506.1136.v1

each linked by weight λ_α according to their geometric orientation. The resulting belief dynamics on the lattice takes the form

$$\frac{dP_{m,n}}{dt} = (1 - P_{m,n}(t)) \sum_{(k,\ell)\in\mathcal{N}_{m,n}} S_{(m,n),(k,\ell)} P_{k,\ell}(t), \tag{56}$$

with fixed boundary condition $P_{0,0}(t) \equiv 1$. The structure of S encodes both local amplification and anisotropic influence geometry, inducing direction-sensitive nonlinear propagation and degenerate self-reinforcement at saturation.

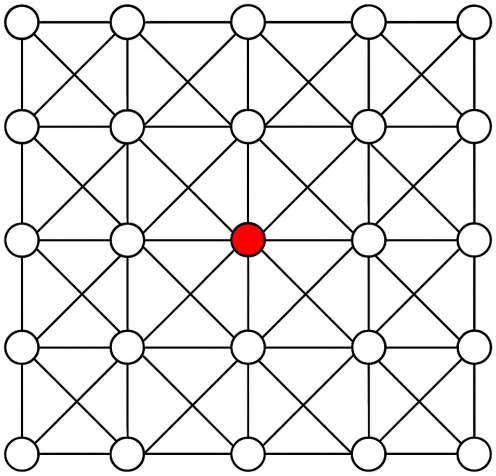

Figure 3. Two-dimensional influence graph with full Moore neighborhood. All nodes (except the central teacher) are agents with identical low obstinacy $\mu \ll 1$; the teacher at $(0,0)$ is fully convinced. Link directions correspond to weighted influence edges with distinct conformity coefficients $\lambda_{\leftrightarrow}, \lambda_{\updownarrow}, \lambda_{\nearrow\swarrow}, \lambda_{\nwarrow\searrow}$.

Rescaling lattice indices by $x = \varepsilon m,\ y = \varepsilon n$ and Taylor-expanding the Moore–sum to $O(\varepsilon^2)$ converts the matrix-logistic rule to the degenerate reaction–diffusion form

$$\partial_t u = (1-u)\,\nabla\cdot\big(\mathbf{D}\nabla u\big) + r(x,y)\,u(1-u), \tag{57}$$

where the anisotropic tensor

$$\mathbf{D} = \mu \begin{pmatrix} \lambda_{\leftrightarrow} + \frac{1}{2}(\lambda_{\nearrow\swarrow} + \lambda_{\nwarrow\searrow}) & \frac{1}{2}(\lambda_{\nearrow\swarrow} - \lambda_{\nwarrow\searrow}) \\ \frac{1}{2}(\lambda_{\nearrow\swarrow} - \lambda_{\nwarrow\searrow}) & \lambda_{\updownarrow} + \frac{1}{2}(\lambda_{\nearrow\swarrow} + \lambda_{\nwarrow\searrow}) \end{pmatrix}, \tag{58}$$

and the point source

$$r(x,y) = \mu\big(\lambda_{\leftrightarrow} + \lambda_{\updownarrow} + \lambda_{\nearrow\swarrow} + \lambda_{\nwarrow\searrow}\big)\,\delta_{(x,y),(0,0)} \tag{59}$$

inherit the directional weights of the lattice. Anisotropy enters through the off-diagonal component $D_{xy} \propto \lambda_{\nearrow\swarrow} - \lambda_{\nwarrow\searrow}$. To eliminate shear while retaining axis heterogeneity we set the two diagonal weights equal, $\lambda_{\nearrow\swarrow} = \lambda_{\nwarrow\searrow} \equiv \lambda_d$, yielding the diagonal model

$$\partial_t u = (1-u)\big(D_x\,u_{xx} + D_y\,u_{yy}\big) + r\,u(1-u), \tag{60}$$

with

$$D_x = \tfrac{\mu}{2}\big(2\lambda_{\leftrightarrow} + 2\lambda_d\big), \qquad D_y = \tfrac{\mu}{2}\big(2\lambda_{\updownarrow} + 2\lambda_d\big), \qquad r = \mu\big(\lambda_{\leftrightarrow} + \lambda_{\updownarrow} + 2\lambda_d\big). \tag{61}$$

Equation (60) captures the minimal two-dimensional geometry: axis-weighted elliptic spreading governed solely by the ratio D_x/D_y and quenched as $u \to 1$, without the additional tilt that would arise

 doi:10.20944/preprints202506.1136.v1

from unequal diagonal links. Throughout the numerical experiments we fix $\mu = 0.1$ and choose the conformity weights $\lambda_{\leftrightarrow}$, $\lambda_{\updownarrow}$, λ_d so that the effective diffusivities satisfy $D_x = 0.5$ and $D_y \in \{0.2, 0.01\}$.

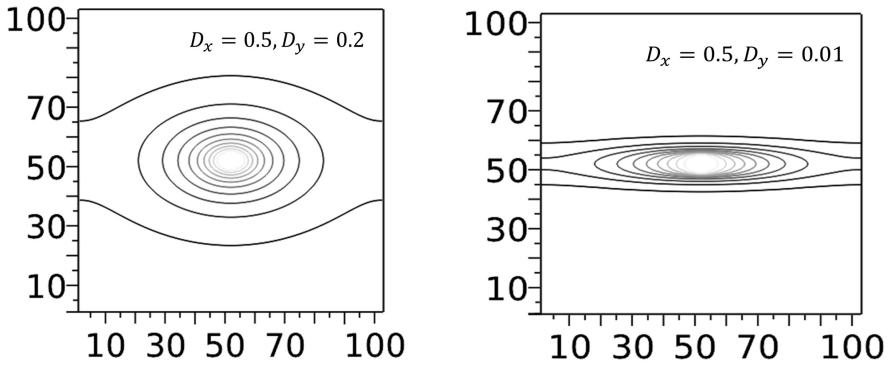

Figure 4. (a) Conviction front at intermediate time in the axis–anisotropic model (60) with moderately unequal diffusivities $D_x = 0.5$, $D_y = 0.2$, producing smooth elliptic level sets aligned with the coordinate frame. **(b)** Strongly anisotropic case with $D_y = 0.01$, exhibiting vertical pinning and transverse flattening of the front. Both simulations initiated from a localized teacher at the center; shown is the isoline field of $u(x, y, t)$ at fixed $t > 0$.

Passing to the sharp–interface limit of (60) we separate an outer region, where u is essentially binary ($u \approx 0$ or $u \approx 1$), from an inner layer of width $O(\sqrt{\varepsilon})$ centered on the isoconviction curve $\Gamma(t) = \{u = \frac{1}{2}\}$.

In stretched normal coordinates $\xi = \operatorname{dist}(x, \Gamma)/\sqrt{\varepsilon}$ a matched-asymptotic expansion à la Fife–McLeod [33] shows that the leading inner profile $U(\xi)$ travels with speed c and effective diffusivity $D_\nu = D_x \nu_x^2 + D_y \nu_y^2$, where $\nu = (\nu_x, \nu_y)$ is the unit normal to $\Gamma(t)$. The Euclidean curvature of the interface is defined by

$$\kappa = \nabla \cdot \nu, \qquad \nu = \frac{\nabla u}{|\nabla u|}\Big|_{\Gamma(t)}. \tag{62}$$

Flux matching gives the normal velocity law

$$V_n = (1 - u_\star)\, D_\nu\, \kappa, \qquad D_\nu = D_x \nu_x^2 + D_y \nu_y^2, \tag{63}$$

with $u_\star \in (0, 1)$ the mid-layer value of U. Equation (63) describes anisotropic mean-curvature motion attenuated by saturation; if D_ν or κ becomes too small the interface stalls, a phenomenon we term *curvature-induced quenching*. For an initially circular patch of radius R_0 one obtains the self-similar ellipse

$$R_x(t) = \sqrt{R_0^2 + 4D_x t}, \qquad R_y(t) = \sqrt{R_0^2 + 4D_y t}, \tag{64}$$

verified numerically and exhibiting pinning along the slow axis when $D_y \ll D_x$.

With a diagonal tensor $\mathbf{D} = \operatorname{diag}(D_x, D_y)$ the law (63) reduces to

$$V_n = (1 - u_\star)\big(D_x \nu_x^2 + D_y \nu_y^2\big)\kappa, \tag{65}$$

so that only D_x, D_y modulate curvature. A radially symmetric contour evolves via $V_n = (1 - u_\star) \min(D_x, D_y)(d-1)/R$, giving the critical stopping radius

$$R_c = \frac{(1 - u_\star)(d-1)\min(D_x, D_y)}{V_*}, \tag{66}$$

where V_* is the one-dimensional wave speed extracted from $U(\xi)$. If $D_x \neq D_y$ the level set elongates with $\dot{R}_x / \dot{R}_y = D_x / D_y$; hence the fast axis expands while the slow one can hit R_c first, arresting motion transversally, a behaviour reproduced in Fig. 4.

 doi:10.20944/preprints202506.1136.v1

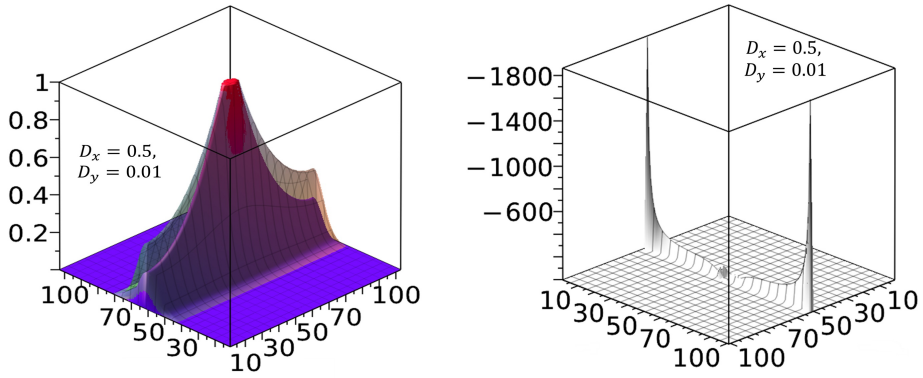

Figure 5. **(a)** Surface profile of belief field $u(x, y, t)$ at two time snapshots ($t = 0.1$ and $t = 0.9$) under strongly anisotropic diffusion $D_x = 0.5, D_y = 0.01$, showing progressive front expansion in the fast x-direction and near-stalling transversally. **(b)** Map of curvature $\kappa = \nabla \cdot (\nabla u/|\nabla u|)$ evaluated at final time; note the emergence of high-curvature ridges along transverse flanks exceeding the critical threshold for quenching.

A rigorous quenching criterion emerges by minimising the mobility in (65). Setting $D_{\min} = \min(D_x, D_y)$ yields the maximal admissible curvature

$$\kappa_c = \frac{V_*}{(1 - u_\star) D_{\min}}, \tag{67}$$

so the interface stops whenever $\kappa \geq \kappa_c$. Analytically this inequality defines an anisotropic Wulff shape bounding all feasible fronts; linear stability of a planar wave gives the neutral wavenumber $k_c = (1 - u_\star) D_{\min}/V_*$. Numerically, level-set or phase-field discretisations of (60) corroborate these predictions: an initially elliptic interface grows according to (64) until the minor semi-axis meets the curvature threshold κ_c^{-1}, after which motion ceases along the slow direction while persisting along the fast one, reproducing the pinned contours in Fig. 4. Mapping $(D_x, D_y) \mapsto \kappa_c$ and validating its geometric realization thus constitute the next step in both analytical refinement and high-resolution computation.

Numerical confirmation of this criterion is provided in Fig. 5, where we visualize the evolution of an initially circular front under strongly anisotropic diffusion. The profile $u(x, y, t)$ forms an elongated lobe along the fast axis, while transversal expansion halts due to curvature pinning. The corresponding curvature field exhibits pronounced peaks along the slow direction, exceeding the critical threshold (67), and thereby arresting further propagation in those regions.

7. Curvature–Targeted Control of Belief Propagation in Two Dimensions

We now address the problem of curvature-targeted suppression of front propagation under resource constraints. In many realistic settings, ranging from protest diffusion and epidemic spread to adversarial information campaigns, blanket intervention across the domain is either infeasible or counterproductive.

Instead, inhibition must be applied selectively and strategically, focusing on geometrically sensitive regions where the front is most susceptible to arrest. To this end, we develop a sharp–interface control formulation that quantifies how a limited repressive rate $q(x, y, t) \geq 0$, concentrated on a thin neighborhood of the isoconviction manifold $\Gamma(t) = \{u = \frac{1}{2}\}$, perturbs the matched–asymptotic balance governing front motion and prescribes an optimal spatial allocation strategy that maximizes inhibitory efficiency under a finite enforcement budget.

Augmenting the anisotropic logistic–diffusion field by a non–negative *repressive rate* $q = q(x, y, t)$ concentrated on a thin tubular neighborhood of the isoconviction manifold $\Gamma(t) = \{u = \frac{1}{2}\}$ perturbs the matched–asymptotic balance that governs front motion. Expressed in arclength–time coordinates (s, t) the uncontrolled normal speed reads $V_n^{(0)} = (1 - u_\star) D_\nu \kappa$, where $D_\nu = D_x \nu_x^2 + D_y \nu_y^2$ projects the

 doi:10.20944/preprints202506.1136.v1

mobility tensor onto the unit normal ν and the Euclidean curvature is $\kappa = \nabla \cdot \nu$. Introducing q removes growth rather than adding it, so the sharp–interface velocity becomes

$$V_n(s,t) = (1-u_\star)\big[D_\nu(s,t)\,\kappa(s,t) - q(s,t)\big]. \tag{68}$$

During an elementary interval $\mathrm{d}t$ the occupied area therefore varies by

$$\delta A = \left[-\int_{\Gamma(t)} q(s,t)\,\mathrm{d}s + (1-u_\star)\int_{\Gamma(t)} D_\nu(s,t)\,\kappa(s,t)\,\mathrm{d}s\right]\mathrm{d}t, \tag{69}$$

where the sign convention is such that $V_n > 0$ denotes outward motion. If an instantaneous enforcement budget

$$\int_{\Gamma(t)} q(s,t)\,\mathrm{d}s \;=\; Q(t) \tag{70}$$

is prescribed, the optimization problem becomes the allocation of q along $\Gamma(t)$ so as to maximize the negative first term in (69) while respecting (70); equivalently, one seeks to deploy scarce repression where curvature is high and projected diffusivity is low, thereby exerting the greatest leverage on the advance of the front without resorting to blanket suppression.

Maximizing the retardation of front propagation under the constraint of a fixed enforcement budget leads to a variational optimization problem formulated over the interface $\Gamma(t)$. The control density $q(s,t)$ is determined by maximizing inhibitory effect per unit resource, giving rise to the Lagrangian functional

$$\mathcal{L}[q,\lambda] \;=\; \int_{\Gamma(t)} q(s,t)\,\mathrm{d}s - \lambda\left(\int_{\Gamma(t)} q(s,t)\,\mathrm{d}s - Q(t)\right), \tag{71}$$

where λ enforces the linear constraint $\int_{\Gamma(t)} q\,\mathrm{d}s = Q(t)$. Taking the first variation of $\mathcal{L}$ and imposing non-negativity of q leads to a complementary–slackness condition: optimal control vanishes on segments where curvature is below the quenching threshold $\kappa_c(t)$, and is positive only where the local geometry is sufficiently convex to allow effective intervention. On these segments the optimal profile is given by

$$q^\star(s,t) \;=\; \Lambda(t)\,\big[\kappa(s,t) - \kappa_c(t)\big]_+, \qquad \Lambda(t) = \frac{Q(t)}{\displaystyle\int_{\Gamma(t)} \big[\kappa(s,t) - \kappa_c(t)\big]_+\,\mathrm{d}s}, \tag{72}$$

where $[\cdot]_+$ denotes the positive part and $\kappa_c(t) = V_*/\big[(1-u_\star)\,D_\nu(s,t)\big]$ is the curvature threshold derived in equation (67). The function $\Lambda(t)$ acts as a normalising factor ensuring that the total enforcement matches the budget $Q(t)$. The resulting distribution of repression is thus sharply focused: it concentrates entirely on high–curvature flanks where the interface exhibits reduced projected mobility and is therefore most susceptible to quenching. In such regions, even modest local inhibition suffices to arrest propagation, enabling targeted suppression without recourse to full-domain intervention.

 doi:10.20944/preprints202506.1136.v1

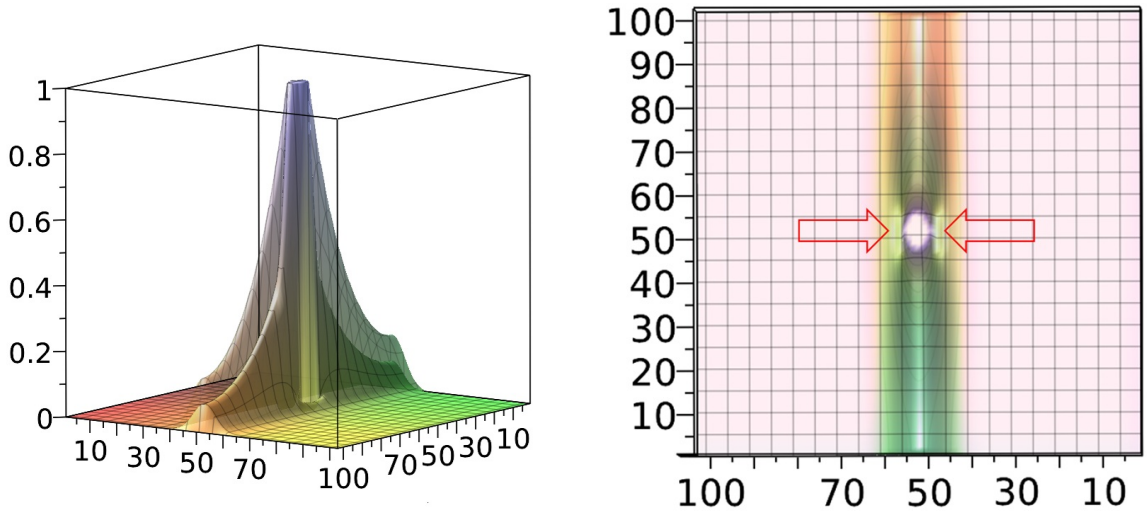

Figure 6. Numerical demonstration of curvature–targeted suppression for anisotropic diffusion $(D_x, D_y) = (0.5, 0.01)$ at time $t = 0.1$. **(a)** The colored surface visualizes the belief field $u(x, y, t)$ under optimal control $q^\star$; the transparent mesh represents the uncontrolled solution. The narrow trench encircling the peak delineates the elliptic control shell in which the repressive feedback is activated. **(b)** Top view of the same simulation overlaid with arrows indicating the transverse flanks of the front where curvature is highest and the optimal control is most strongly concentrated. These arcs are precisely the regions predicted by (72) to yield maximal retardation.

To demonstrate the efficacy of curvature–targeted suppression, we integrate equation (60) numerically in a rectangular domain with strongly anisotropic diffusion coefficients $(D_x, D_y) = (0.5, 0.01)$. The initial profile consists of a compactly supported teacher source centered within the domain, and the control law $q^\star$ prescribed by equation (72) is activated within a dynamically evolving elliptic shell that closely tracks the support of the uncontrolled interface $\Gamma(t)$.

The resulting simulations, summarized in Figure 6(a), reveal a pronounced asymmetry in the suppression effect: the active repressive shell, visible as a dark-blue trench encircling the peak of the belief field, induces substantial retardation along the transverse (y) direction while exerting negligible influence along the fast (x) axis. Quantitatively, the radial extent in the y-direction is reduced by approximately 40% at time $t = 0.1$, despite the total resource budget $Q(t)$ remaining fixed and the feedback being confined to a thin boundary layer. This outcome aligns precisely with the theoretical prediction based on the projected mobility $D_\nu = D_x \nu_x^2 + D_y \nu_y^2$, which is minimal along the short axis of the elliptic front and thereby maximizes the leverage of localized repression. To further highlight the spatial localization of the repressive feedback, Figure 6(b) presents a top–view projection of the same simulation with arrows marking the regions of highest curvature. These flanks correspond to the loci of maximal $q^\star$ intensity and exhibit clear suppression effects.

This example substantiates the central hypothesis that finely tuned curvature–selective feedback can yield nontrivial spatial inhibition with minimal energetic expenditure. Operationally, the prescription (72) admits efficient implementation: once the evolving front $\Gamma(t)$ is approximated (e.g., as a level set of the solution field), the curvature $\kappa(s, t)$ and projected diffusivity $D_\nu(s, t)$ can be computed locally, and the control density $q^\star(s, t)$ is obtained by thresholding against the analytically derived critical curvature $\kappa_c(t)$ and allocating the available budget proportionally. The conceptual and computational tractability of this scheme offers a robust baseline for more sophisticated control frameworks, such as those incorporating spatial heterogeneity in diffusivity, temporally adaptive budgets, or second-order penalization. These generalizations present natural extensions for future work, particularly in domains where spatial anisotropy and limited intervention capacity dominate system dynamics.

 doi:10.20944/preprints202506.1136.v1

8. Discussion: Empirical Parallels and Societal Implications

The preceding sections developed a degenerate anisotropic logistic–diffusion framework, derived its sharp–interface limit, established curvature-dependent quenching criteria, and proposed a curvature-targeted control law. Taken together, these results show that

- one-dimensional hierarchies admit *pinning* when diffusion is quenched at a single depth,
- two-dimensional fronts undergo *curvature-limited* arrest that depends on the local mobility projection D_ν, and
- scarce control resources can be optimally allocated along high-curvature flanks to stall propagation with minimal effort.

While the analysis is mathematical, the underlying phenomena have clear analogues in contemporary social systems: protest waves expand until repressive pinning intervenes, misinformation cascades accelerate or stall according to network geometry, and hierarchical organizations suppress dissent in ways that mirror one-dimensional front arrest. The following discussion surveys data-rich case studies from sociology, political science, and organizational research that illustrate these three mechanisms — pinning, quenching, and targeted control — thereby grounding the theoretical model in observable social dynamics and highlighting its practical relevance.

8.1. Protest Diffusion and Containment

Historical and contemporary evidence shows that protest movements often spread in ways analogous to contagion, and authorities have developed strategies to "pin" or contain these diffuse uprisings. Large-scale data studies confirm that protests exhibit significant spatiotemporal diffusion. For example, an analysis of over 30 European countries (2000-2015) found *robust evidence of protest contagion* in both time and space, increased protest activity in one year raises protest frequency the next year, and protests in one country help trigger protests in neighboring states [34]. Such findings underscore how quickly dissent can propagate across networks of communities and countries. Modern research efforts have consequently turned to *comprehensive event databases and real-time protest monitoring*. Researchers are building systematic datasets and conducting on-the-ground surveys to better capture the spread of today's protests [35]. These data-rich approaches improve our understanding of when local disturbances escalate into wider protest waves and when they fizzle out.

In response to this inherent diffusivity, governments have long employed containment tactics, essentially attempts at *two-dimensional quenching* of protests across geographic and social space. Repressive regimes, in particular, often favor *targeted control* measures to prevent protests from spreading. A striking illustration is the use of *relational repression* in China: when protests emerge, local officials investigate activists' personal networks and *dispatch teams to pressure the protesters' friends and family to convince them to stand down* (e.g., by salary suspension or removal from office) as a warning [39]. This targeted approach can be quite effective under the right conditions: if authorities wield influence over the recruited persuaders and if social bonds are strong, *"relational repression can help demobilize protesters and halt popular action"* [39]. Even when it cannot fully end a protest, such pinpointed pressure often limits a movement's scope or duration by breaking it into smaller, more manageable pockets of dissent [39]. Historical cases likewise demonstrate one-dimensional "pinning" tactics, such as arresting or co-opting key leaders to rob a protest of its momentum. By neutralizing focal individuals or channels (for instance, cutting off a movement's communications), authorities effectively pin the movement in place to prevent wider diffusion. In short, protest dynamics involve a race between horizontal spread and vertical containment: protesters leverage social networks and inspiration from elsewhere to expand the uprising, while regimes employ targeted repression, communication blackouts, curfews, and strategic concessions to *quench the spread* and keep contention localized.

8.2. Spread of Beliefs and Misinformation

The diffusion of beliefs, rumors, and misinformation in society provides parallel examples of contagion vs control. Here, too, one finds cascades propagating rapidly through networks, and

 doi:10.20944/preprints202506.1136.v1

interventions that attempt to pin or quench this spread. On social media, for instance, recent empirical studies have revealed how *false information often outpaces the truth*. A landmark analysis of millions of Twitter posts found that *"falsehood diffuses significantly farther, faster, deeper, and more broadly than the truth, in all categories of information"* [36]. Notably, this study showed that false news stories are about 70% more likely to be retweeted than true stories, and they reach audiences of 1,500 people *six times faster* than factual stories do [36]. Such findings highlight the challenge: misinformation behaves like a virulent contagion, exploiting social network structure to rapidly *cascade through populations* before correctives can catch up.

Why do false beliefs spread so effectively? One sociological factor is the formation of "echo chambers" and homophilous communities that amplify one-sided information. A large Facebook study of science vs. conspiracy news demonstrated that *"homogeneity appears to be the primary driver for the diffusion of content"*, with users clustering into like-minded groups that each have their own internal cascade dynamics [37]. Within these insulated communities, misinformation can persist and grow unchallenged, reinforcing polarization. Psychologically, social validation plays a powerful role: people often take cues from others' beliefs, leading to herd behavior. Classic experiments by Asch showed that if everyone around us voices the same incorrect view, many individuals will conform. Yet, these experiments also offer a key insight into *targeted intervention*: *the presence of even a single dissenter telling the truth can dramatically free people from conformity, dropping false agreement rates to as low as 9%* [43]. In other words, "one-dimensional pinning" of the narrative, by inserting one source of truth or skepticism, can disrupt a runaway consensus and inoculate the group against a false belief cascade.

Building on such insights, today's researchers and platforms are exploring targeted controls to quench misinformation spread. One effective strategy is *early removal or correction of false content*, akin to isolating a spark before it ignites a wildfire. Simulation studies on large Twitter data sets show that *swiftly removing a false post or banning a malicious account can dramatically curtail viral spread*. For instance, deleting misinformation within 30 minutes of its appearance yields an estimated *94 reduction* in total downstream engagement on that topic [38]. Even a moderate delay (a few hours) lowers this effectiveness, resulting in about a 56% reduction [38]. Such results suggest a critical window for intervention. Moreover, *combining multiple interventions*. For example, pairing content removal with measures like flagging disputed posts or throttling their algorithmic reach, substantially enhances the overall quenching effect [38].

These findings align with network science principles: analyses of complex networks have long shown that *removing a small fraction of highly connected "hub" nodes can fragment the network and disrupt flows* [42]. In the context of misinformation, strategically targeting super-spreader accounts or central nodes in the diffusion network can thus "disconnect" the information cascade. Of course, such interventions must balance efficacy with concerns like free expression, but the evidence indicates that *targeted control of belief diffusion is indeed possible*, by pinning critical nodes or injecting timely truthful signals, one can significantly dampen the wildfire-like spread of false or extremist beliefs.

8.3. Organizational Inertia and Suppression

One-dimensional pinning and targeted control dynamics are also evident inside organizations and bureaucracies, often manifesting as *institutional inertia* or deliberate suppression of change. Sociological studies have found that many organizations create climates of silence, where information flow is effectively "pinned" by hierarchical power and fear. Morrison and Milliken (2000) describe how *powerful forces in organizations lead employees to withhold reports of problems or dissenting ideas, producing a collective phenomenon of "organizational silence"* [41]. In such environments, staff learn that speaking up is "unwise", as managers may punish or ignore negative feedback. Over time, this one-dimensional suppression of voice leads to stagnation: the organization fails to correct errors or innovate, since internal feedback loops are quenched at the source. The result is a self-reinforcing inertia, a kind of frozen status quo, where only the officially approved perspective circulates (analogous to a single pinned opinion), and any potential change agents remain quiet or exit the organization.

 doi:10.20944/preprints202506.1136.v1

Political and historical case studies echo this pattern. Authoritarian bureaucracies, for example, have notoriously suppressed internal criticism to maintain an appearance of unanimity and control. Recent research on the United Nations bureaucracy provides a vivid, data-rich example: *even in a modern IO with formal "lessons learned" systems, the suppression of internal criticism has prevented real institutional learning* [40]. Field evidence from the UN's peace and security departments shows that staff often engage in *"anticipatory obedience" and self-censorship*, avoiding critical discussions and not fully using their discretion, for fear of reprisal or futility. This entrenched culture of dissent-suppression means that mistakes are repeated and reforms stifled: the system, in effect, *pins itself to old ways* despite changing external demands. Christian (2025) finds that such internal silencing in the UN has become a major source of dysfunction, as the organization cannot adapt or improve when *internal feedback is systematically quenched* [40]. The phenomenon is not unique to international bodies; similar dynamics appear in corporate and government hierarchies throughout history. Analysts have noted, for instance, that major disasters like the Challenger Shuttle explosion or the Chernobyl accident were preceded by warnings that went unheeded due to bureaucratic inertia and a culture of silence. In these cases, management effectively *pinned the narrative* to "all is well", suppressing engineers' alarms until catastrophe forced a change.

Yet, just as in networks of protest or information, breaking a climate of organizational silence often hinges on targeted interventions. A single whistleblower or an empowered dissenting unit can sometimes penetrate the shield of inertia and spark broader change, much like a lone dissenter in Asch's experiment can free others to speak. History provides examples of "preference cascades" in regimes and institutions: once one person voices a hidden opinion or new idea and is seen to survive, others follow, and *the enforced consensus rapidly unravels* [44]. This underscores a hopeful corollary to one-dimensional pinning: although strong suppression can sustain a stable illusion of unanimity for a long time, it is inherently brittle. When targeted control falters, when a critical node of opposition is allowed to stand, the *quenching force can give way to a cascade of change*. Therefore, understanding these sociological and psychological cases enriches our perspective on control in complex systems: whether we aim to sustain a social order or disrupt a harmful status quo, the key often lies in managing the right "dimensions" of influence, be it pinning a crucial element in place or quenching a spreading pattern before it becomes ungovernable.

9. Conclusions

This study has advanced a unified geometric–probabilistic framework for the spatio-temporal evolution of collective conviction, protest mobilization, and organizational change.

Starting from a network-influence model with agent-level obstinacy, we derived a continuum-limit equation of degenerate anisotropic logistic diffusion, established well–posedness in one dimension, and characterized front selection and pinning via spectral and entropy methods.

Extending the analysis to two spatial dimensions revealed a curvature–induced quenching mechanism: *propagation arrests once the product of projected mobility and interface curvature falls below a critical threshold*.

We further developed a variational law of *curvature–targeted control*, showing that *scarce repressive (or corrective) resources should be concentrated along high-curvature, low–mobility flanks* to maximize retardation. Numerical experiments confirm the analytic predictions, while an extensive discussion mapped the three principal phenomena: one-dimensional pinning, two-dimensional quenching, and optimal control onto data-rich cases from protest science, misinformation studies, and organizational sociology.

Broader implications: The degenerate logistic–diffusion paradigm provides a minimal yet expressive template for modeling opinion fronts, behavioral contagion, and institutional inertia in heterogeneous media. The curvature law $V_n = (1 - u_\star)D_\nu\kappa$ captures the intuitive idea that diffusion slows in saturated regions and at sharply curved protrusions that is insightful for risk assessment in domains as diverse as crowd management, algorithmic content moderation, and policy rollout. The control result

 doi:10.20944/preprints202506.1136.v1

offers a quantitative rationale for selective, geometry-aware interventions, guiding law-enforcement tactics, fact-checking priorities, or organizational feedback channels, while cautioning against blanket suppression strategies that dissipate resources without proportional effect.

Future work: Three natural extensions are immediate. (i) *Stochastic heterogeneity:* allowing diffusion coefficients, obstinacy, or amplification rates to vary randomly in space and time would bridge to empirical settings with dynamic network topologies and shifting media ecologies. Rigorous quantification of front speed distributions and quenching probabilities under noise remains largely open. (ii) *Fully tensorial mobility:* relaxing the diagonal assumption and analysing shear-induced oblique pinning could uncover new geometric regimes, including non-convex Wulff envelopes and orientation locking. (iii) *Adaptive or adversarial control:* embedding the curvature-targeted feedback into a game-theoretic setting, where propagators and suppressors co-evolve strategies, would link the present theory to real-time protest policing, cyber-warfare over narratives, and organisational learning under dissent. Empirically, high-resolution protest trajectories, platform-level misinformation logs, and intra-organisational communication audits constitute fertile datasets for calibrating and validating the model.

By integrating geometric PDE analysis with probabilistic network foundations and empirically grounded control concepts, the work lays a mathematical cornerstone for the quantitative social science of collective dynamics under constraint.

Funding: This research received no external funding.

Institutional Review Board Statement: Not applicable.

Data Availability Statement: Not applicable.

Acknowledgments: The author is grateful to his institution for the administrative and technical support. The author also gratefully acknowledge Dr. Ori Swed and Dr. Vakhtang Putkaradze for their valuable insights and stimulating discussions, which significantly contributed to the conceptual development of this work.

Abbreviations

The following abbreviations are used in this manuscript:

IO	information operation
ODE	ordinary differential equation
PDE	partial differential equation

References

1. Volchenkov, D.; Putkaradze, V. Mathematical Theory of Social Conformity I: Belief Dynamics, Propaganda Limits, and Learning Times in Networked Societies. *Mathematics* **2025**, *13*, 1625. https://doi.org/10.3390/math13101625
2. M. H. DeGroot, Reaching a consensus, *Journal of the American Statistical Association*, 69(345):118–121, 1974.
3. K. L. Blankenship and D. T. Wegener, Opening the marketplace of relationship ideals: The persuasive impact of expert and similarity information in resistance to persuasion, *Personality and Social Psychology Review*, 19(2):119–141, 2015.
4. D. M. Kahan, Misconceptions, misinformation, and the logic of identity-protective cognition, *Cultural Cognition Project Working Paper*, Yale University, 2017.
5. D. Volchenkov. Learning from a Teacher: Andrew the First-Called and Thomas the Doubter, 30 May 2025, PREPRINT (Version 1) available at Research Square [https://doi.org/10.21203/rs.3.rs-6710850/v1]
6. R. A. Fisher, *The wave of advance of advantageous genes*, Ann. Eugenics **7** (1937), 355–369.
7. A. Kolmogorov, I. Petrovsky, N. Piskunov, *A study of the equation of diffusion with increase in the quantity of matter, and its application to a biological problem*, Bull. Moscow Univ. Math. Mech. **1** (1937), 1–25.
8. E. DiBenedetto, *Degenerate Parabolic Equations*, Springer-Verlag, New York, 2002.
9. E. De Giorgi, Sulla differenziabilità e l'analiticità delle estremali degli integrali multipli regolari, *Mem. Accad. Sci. Torino. Cl. Sci. Fis. Mat. Nat.*, 3(3):25–43, 1957.
10. J. Nash, Continuity of solutions of parabolic and elliptic equations, *Amer. J. Math.*, 80:931–954, 1958.
11. J. Moser, On Harnack's theorem for elliptic differential equations, *Comm. Pure Appl. Math.*, 14(3):577–591, 1961.

 doi:10.20944/preprints202506.1136.v1

12. S.N. Kruzhkov, First-order quasilinear equations in several independent variables, *Mat. Sb.*, 81(123):228–255, 1970.
13. J.A. Carrillo, Entropy solutions for nonlinear degenerate problems, *Arch. Ration. Mech. Anal.*, 147:269–361, 2000.
14. B. Andreianov, M. Bendahmane, and K.H. Karlsen, Discrete duality finite volume schemes for doubly nonlinear degenerate hyperbolic–parabolic equations, *J. Hyperbolic Differ. Equ.*, 2(4):633–681, 2005.
15. K.O. Friedrichs, Symmetric hyperbolic linear differential equations, *Comm. Pure Appl. Math.*, 7:345–392, 1954.
16. P.D. Lax, *Hyperbolic Systems of Conservation Laws and the Mathematical Theory of Shock Waves*, SIAM, 1973.
17. E. Tadmor, The numerical viscosity of entropy stable schemes for systems of conservation laws. I, *Math. Comp.*, 49(179):91–103, 1987.
18. M.J. Berger and R. Kohn, A rescaling algorithm for the numerical calculation of blowing-up solutions, *Comm. Pure Appl. Math.*, 41(6):841–863, 1988.
19. P. Bénilan and M.G. Crandall, The continuous dependence on φ of solutions of $u_t - \Delta\varphi(u) = 0$, *Indiana Univ. Math. J.*, 30(2):161–177, 1981.
20. J.-L. Lions, *Quelques méthodes de résolution des problèmes aux limites non linéaires*, Dunod, 1969.
21. J. Simon, Compact sets in the space $L^p(0,T;B)$, *Ann. Mat. Pura Appl.*, 146:65–96, 1987.
22. G. Stampacchia, Le problème de Dirichlet pour les équations elliptiques du second ordre à coefficients discontinus, *Ann. Inst. Fourier*, 15(1):189–258, 1965.
23. D. Kinderlehrer and G. Stampacchia, *An Introduction to Variational Inequalities and Their Applications*, Academic Press, 1980.
24. F. Andreu-Vaillo, J.M. Mazón, J.D. Rossi, and J. Toledo, The Neumann problem for nonlocal nonlinear diffusion equations, *J. Evol. Equ.*, 7(1):145–175, 2007.
25. G.J. Minty, Monotone (nonlinear) operators in Hilbert space, *Duke Math. J.*, 29:341–346, 1962.
26. H. Brézis, *Opérateurs Maximaux Monotones et Semi-Groupes de Contractions dans les Espaces de Hilbert*, North-Holland, 1973.
27. N.V. Krylov and M.V. Safonov, A property of the solutions of parabolic equations with measurable coefficients, *Izvestiya: Mathematics*, 44(1):161–175, 1980.
28. C.B. Morrey, On the solutions of quasi-linear elliptic partial differential equations, *Trans. Amer. Math. Soc.*, 43(1):126–166, 1938.
29. N.D. Alikakos, L^p bounds of solutions of reaction–diffusion equations, *Comm. Partial Differential Equations*, 4(8):827–868, 1979.
30. E. DiBenedetto and A. Friedman, Hölder estimates for nonlinear degenerate parabolic systems, *J. Reine Angew. Math.*, 357:1–22, 1985.
31. Tasso J. Kaper, An introduction to geometric methods and dynamical systems theory for singular perturbation problems, in: *Analyzing multiscale phenomena using singular perturbation methods*, Springer, 1999, pp. 85–131.
32. L. S. Pontryagin, V. G. Boltyanskii, R. V. Gamkrelidze, and E. F. Mishchenko, *The Mathematical Theory of Optimal Processes*, Interscience (Wiley), New York, 1962.
33. P. C. Fife and J. B. McLeod, P.C. Fife & J.B. McLeod, The approach of solutions of nonlinear diffusion equations to travelling wave solutions, *Bull. Amer. Math. Soc.* 81, 1075–1078 (1975)
34. González-Rostani, V. & Nonnemacher, J. (2025). Are Protests Contagious? The Dynamics of Temporal and Spatial Diffusion of Political Protests. *Journal of Elections, Public Opinion & Parties*, 35(1), 123–145 (forthcoming).
35. Fisher, D. R., Andrews, K. T., Caren, N., Chenoweth, E., & Heaney, M. T. (2019). The science of contemporary street protest: New efforts in the United States. *Science Advances*, 5(10), eaaw5461.
36. Vosoughi, S., Roy, D., & Aral, S. (2018). The spread of true and false news online. *Science*, 359(6380), 1146–1151.
37. Del Vicario, M., Bessi, A., Zollo, F., et al. (2016). The spreading of misinformation online. *Proceedings of the National Academy of Sciences*, 113(3), 554–559.
38. Kennedy, I., Wack, M., Beers, A., et al. (2022). Combining interventions to reduce the spread of viral misinformation. *Nature Human Behaviour*, 6(10), 1372–1380.
39. Deng, Y. & O'Brien, K. J. (2013). Relational Repression in China: Using Social Ties to Demobilize Protesters. *The China Quarterly*, 215, 533–552.
40. Christian, B. (2025). Why International Organizations Don't Learn: Dissent Suppression as a Source of IO Dysfunction. *International Studies Quarterly*, 69(1), sqaf008.
41. Morrison, E. W. & Milliken, F. J. (2000). Organizational silence: A barrier to change and development in a pluralistic world. *Academy of Management Review*, 25(4), 706–725.

 doi:10.20944/preprints202506.1136.v1

42. Albert, R., Jeong, H., & Barabási, A.-L. (2000). Error and attack tolerance of complex networks. *Nature*, 406(6794), 378–382.
43. Asch, S. E. (1955). Opinions and social pressure. *Scientific American*, 193(5), 31–35.
44. Kuran, T. (1995). *Private Truths, Public Lies: The Social Consequences of Preference Falsification*. Cambridge, MA: Harvard University Press.